

Investigation on Flow Characteristics of Generic Car Body with Different Boundary Conditions

Sinan Keiyinci¹, Oğuz Baş^{2*} and Mustafa Atakan Akar¹

¹ The Faculty of Engineering, Cukurova University Automotive Engineering, Adana, 01380, Turkey

² Faculty of Engineering, Amasya University, Mechanical Engineering, Amasya, 05000, Turkey

*Corresponding author e-mail: oguz.bas@amasya.edu.tr tel: +90 358 2115053

skeiyinci@cu.edu.tr (Sinan Keiyinci)

aakar@cu.edu.tr (Mustafa Atakan Akar)

ABSTRACT

In automotive aerodynamics, it is not common to focus on a specific vehicle due to restricted access to the CAD geometries, their short life span, and limited validation data. For this reason, researchers prefer generic bodies that look like automobiles such as Ahmed Body in their investigations. However, the absence of moving ground and rotating wheels makes these generic bodies unrealistic for aerodynamic studies. In this context, including wheels in CFD simulations, varying ground, and wheel boundary conditions, and comparing their qualitative and quantitative flow parameters with the original Ahmed Body experiment is the main objective of this paper. Results have shown that changing stationary ground and wheel boundaries into moving and rotating boundaries do have minor effects on wake characteristics and drag coefficients. However, just the presence of wheels on the model increases force coefficients significantly (increment in drag and lift coefficients by 27.32% and 188.5 counts, respectively.) even though these boundaries are stationary. As a result, the absence of moving ground and rotating wheels can be tolerated to some extent (especially for experimental studies in which inclusion of moving and rotating boundaries may have difficulties). However, a study cannot be evaluated exactly with a model without wheels.

Keywords: Drag; Lift; External Aerodynamics; Turbulence; CFD; Ahmed Body

1. INTRODUCTION

Decreasing fuel consumption is the main concern in the automotive industry to save energy and pollute the environment less. Generally, there are several approaches to enhance fuel economy such as improving the performance of the engine, reduction of the vehicle weight, and minimizing the aerodynamic drag. Approximately 50-70% of the total power is consumed to overcome the aerodynamic drag by a vehicle at 100 km/h [1]. Moreover, the aerodynamic power consumption is proportional to the cube of the vehicle velocity so investigations on the related topic have shown that a drop of 10% in the drag coefficient can decrease fuel consumption by about 5% [2].

An interest has aroused in automotive aerodynamics following the petroleum crisis in the 70s. According to the authors' knowledge, Morel [3] and Ahmed [4] were the first researchers that revealed the significance of the slant angle of a bluff body that is similar to a vehicle. Since Ahmed and his colleagues demonstrated a simple model known as Ahmed Body in 1984, the model is now one of the most studied generic bodies in the automotive aerodynamics literature. Despite the model being quite similar to that Morel's body in 1978, the Ahmed body has a slightly longer and thinner shape which makes it more suitable for automotive aerodynamic investigations due to its closer family-car proportions.

Ahmed body is generic vehicle geometry has a rounded flat front and a slanted rear upper surface. The slant angle is a variable and one of the most frequently studied parameters for this body [4–7]. These studies pointed out that the aerodynamic forces, the strength of the flow separation, and wake structure highly depend on the slant angle. A considerable drag peak is observed at the slant angle of 30°. This angle results in such a drag peak that it is now termed the critical slant angle. The flow is fully detached over the slant surface due to a strong adverse pressure gradient between the roof and slant higher angle values than 30° of slant angle [8]. Besides, the drag force exerted on the body is mainly because of the pressure drag that is generated at the rear end. The rear part of the body generates such a separation zone and counter-rotating vortices that it increases the complexity of the wake structure.

However, most of the studies on Ahmed body till Strachan et al. [9] were more unrealistic compared with ground vehicles because of the absence of moving ground and wheels effect. Their experimental investigation has been shown that the inclusion of the moving ground has little effect on the drag coefficient and formation of counter-rotating longitudinal vortices that are formed over the top of the model. On the other hand, the addition of wheels to the Ahmed body has a significant effect on aerodynamic forces according to numerical investigations of [10]. It was found that the addition of the wheel and wheelhouses on the Ahmed body caused the average drag and lift increment up to 0.058 and 0.243, respectively [11].

On the other hand, adding rotating wheels and moving grounds on a wind or water tunnel is a tough mission and might result in a high cost for researchers. Although there are various studies focusing on the effects of ground floor motion [12,13], wheel addition [14,15], and wheel rotation [16,17] with different models and setups in the aerodynamic literature, there is no comprehensive and comparative study of the effects of changing these boundary conditions covering all scenarios.

In this context, including moving ground and rotating wheels in CFD (Computational Fluid Dynamics) simulations and comparing their qualitative and quantitative flow parameters extensively with the original Ahmed Body experiment is the main objective of this paper. Besides, different setups of stationary wheels and ground combinations were also investigated to

assess their motion effects on the flow structure. In this numerical study, poly-hexcore meshed CFD setups were solved with a $k-\omega$ SST turbulence model.

2. NUMERICAL APPROACH

2.1. CAD Model

The CAD (Computer Aided Design) models were created with SpaceClaim V19 software. While there are four configurations used in simulations, namely; Ahmed body with the stationary ground (SG), Ahmed Body with moving ground (MG), Ahmed body with stationary wheels and ground (SW+SG), Ahmed body with moving ground and stationary wheels (SW+MG) and Ahmed body with moving ground and wheel (MW+MG), two different CAD models were generated; Ahmed Body with wheels and without wheels since just switching the ground and wheel boundaries of the SG and SW+SG configurations from the stationary wall to the moving wall type without a geometric modification is enough for the MG, SW+MG and MW+MG simulations. Whereas the CAD model of the SG and MG simulations are the same as Ahmed's original Body in 1984, wheel-included geometric configurations are adopted from the numerical study of Huminic and Huminic [11]. The dimensions and details of the Ahmed Body with the wheels are shown in Figure 1.

2.2. Mesh Generation and Mesh Independence

The main purpose of grid optimization is to reach the best accuracy by the available computational resource. In the present work, a grid generation strategy was carried out to minimize the number of mesh elements in the free stream and far region and to maximize them downstream close to the body and near-wall regions. Watertight Geometry Workflow of Ansys Fluent 2019 R3 CFD software was used as a meshing tool to achieve this purpose. Besides, Ansys new Mosaic meshing technology was utilized to obtain high-quality mesh that provides high accuracy and easy convergence with minimum element size. Moreover, the volume and surface mesh improvement skills of the meshing tool were utilized to ensure the high quality of the mesh. As a result, throughout the simulations, all numerical setups ensured an orthogonal quality higher than 0.2.

The mesh structure has two refinement boxes that have denser mesh than global elements to capture flow characteristics better for the near regions of vehicle, underbody, and wake (Figure 2). To take full advantage of the $k-\omega$ SST turbulence model, the wall adjacent cell heights were kept $y^+ < 5$ at all stationary (no-slip) walls for all numerical setups. In line with this strategy, 24 prism layers were used to capture the turbulent boundary layer as much as possible.

To satisfy mesh independence, four different mesh sizes were created by improving the element size of refinement boxes: Mesh 1 (coarse), Mesh 2 (medium), Mesh 3 (fine), and Mesh 4 (very fine). The grid refinement strategy was executed for all regions of the domain as can be seen in Table 1. These meshes were tested for SG setup. Fine (Mesh 3) mesh size was chosen for the rest of the study amongst them which satisfies variation of C_D and C_L lower than 2.4 and 1.3 counts (1 count=0.001), respectively. The results of the mesh independence study are shown in Figure 3.

2.3. Turbulence Model

In this study, an incompressible, steady-state RANS approach has been adopted. As turbulence models, Menter's $k-\omega$ Shear Stress Transport (SST) [18] that have been widely used and validated in the literature [11,19–22] was utilized.

The model is a two-equation model that provides a solution to the RANS with a reasonable degree of accuracy at a reasonable computational expense. Despite Detached Eddy Simulations (DES), Large Eddy Simulations (LES), and Unsteady Reynolds-Averaged Navier-Stokes (URANS) ensure more accuracy for the flow field this would probably require much increased computational cost and power and hence, is out of the scope of this investigation. Furthermore, Guilmineau et al. [20] reported that for the Ahmed body slant angle of 35° , the majority of RANS turbulence models capture flow properties correctly and give a good agreement with the experimental data. Siddiqui and Chaab used the same turbulence model with the 35° slanted rear-ended Ahmed body with good accuracy [19]. For this reason, an Ahmed body with a slant angle of 35° was used during all simulation setups.

2.4. Boundary Conditions, Solver Settings, and Post Processing

For numerical simulations, RANS equations were solved with pressure-based (gravitational effects neglected), steady-state, adiabatic, fully turbulent flow properties. At the inlet, reference pressure and temperature values of air were set $p_\infty = 1$ atm $t_\infty = 15^\circ\text{C}$, respectively.

The freestream velocity was maintained to $V_\infty = 40$ m/s which is corresponding to a Reynolds number $Re_\infty = 2.78 \times 10^6$ (based on Ahmed body length, $l = 1.044$ m) and the turbulence intensity was 0.5 % at the velocity inlet. The pressure outlet was set to a gauge pressure of 0 Bar with 5% turbulence intensity at the exit.

A flow domain must be defined sufficiently large to attain accurate numerical solutions. The computational domain is designed as a box to get a stable inlet flow and a fully developed wake flow. For more detail, schematic representation of the numerical domain, boundary conditions setups, and domain properties for numerical configurations of this study are presented in Figure 4, Table 2, and Table 3 respectively.

3. RESULTS

3.1. Validation

Force coefficient results of simulations of this study with different boundary setups are compared with experimental results of [4,7,9] and numerical results of [11] in Table 4. The values of Ahmed et al. [4] experimental work were obtained at 4.29 million Reynolds number based on body length which is corresponding to a free stream velocity $U_\infty = 60$ m/s and this Reynolds number is 1.51 million higher than that used in this paper. The results measured by Meile et al. [7] were acquired with the same Reynolds number used in this investigation which also includes the lift coefficient measurement shown below. In addition, an experimental study of the MG setup of Strachan et al. [9] with a $Re = 1.7 \times 10^6$ and a numerical study of

Huminic and Huminic [11] with the same order Reynolds number of this study are presented. It can be said that the drag prediction of this study for SG is in good agreement with a variation of 8.4 and 12.6 counts compared with the experimental data of [4] and [7], respectively. The deviation of C_D from the experimental measurement of [4] is a result of the lower Reynolds number of this study as reported in [8], while the absence of stilts in the numerical setups is possibly the reason for the underestimation of the C_D comparing with [7]. Despite all, this order of deviation still can be assumed in acceptable engineering limits by some researchers [5,22,23]. Besides, the C_L result for the SG setup of this study is only 1.3 counts higher than the experimental data of Meile et al. which is an acceptable deviation for the lift coefficient. As for the MG setup, the reference experimental data from Strachan et al. [9] deviates 13 counts from this study. This can be attributed lower Reynolds number of that study ($Re=1.7 \times 10^6$). On the other hand, the C_D are reported around 0.275 and 0.28 at $Re=1.42 \times 10^6$ and 2.13×10^6 for the 35° slant angle [22]. This means the inclusion of moving ground results in drag reduction for wheelless Ahmed body around 2% which is quite good agreement with the trend of this study. Regarding MW+MG setup, C_D and C_L coefficients of this study deviate 5.8 and 45.4 counts from the numerical investigation of [11] which has the same geometry as the present study. The main reason for this variation is due to the difference in meshing strategies, according to the authors of this paper. Albeit the same geometry and turbulence model is used, the first cell height on the surfaces of the body is kept $30 < y^+ < 100$ in Huminic and Huminic's study.

Regarding qualitative validation of the numerical study, the normalized x-directional velocity profile (U_x/U_∞) at the line of $y/H=1.065$ located in the symmetry plane ($z=0$) is evaluated for the SG setup. The experimental result of the velocity profiles for the Ahmed body is represented in Figure 5. obtained by Lienhart and Becker [24] which can be obtained from also ERCOFTAC database. It can be seen from graph that the present numerical study is good at predicting trends of velocity profiles at this line. The overpredictions occur near the curved frontal face and the beginning of the slanted edge where flow velocity rises. However, the highest deviation in U_x/U_∞ is 4.47% which is an acceptable range. Consequently, when taking both the qualitative and quantitative validation into account, the present pre-processing and solution setups are accepted validated, and used for the rest of all numerical simulations in this study.

Besides the velocity profile comparison, wake flow topology is verified with streamlines in the symmetry plane ($z = 0$), and the results of the base model are compared with experimental data of Lienhart and Becker's study [24] in Figure 6. It should be considered that Reynolds Number is approximately 25% higher for the relevant experiments than in the current numerical study. In the current study, all characteristic upper Foci (F_1), lower foci (F_2), and saddle point (S) have the same trends as the experimental results. As shown in these figures, the positions of critical points are almost consistent with the experimental data in vertical coordinates (y/h). However, slight differences can be seen for the horizontal positions (x/l) of the points. For the current study, F_1 is further away whereas F_2 and S points are closer to the model compared to experiments. This can be anticipated because of the higher Reynolds number of experimental work. Bluff bodies with a higher back slanted surface are characterized by the domination of upwash and their flow tends to separate from the slanted surface as reported by [25]. Considering a 35° rear slant angle was used in this study, it can be said that downwash domination is reduced due to lower freestream. On the contrary, when the downwash domination is reduced against upwash, F_2 and S move in the downstream direction. It is thought that F_1 is closer to the object, while the points F_2 and S are further away in the downstream direction for these reasons, in the experimental results. Hence, an issue similar to this can be seen in reference [26] if different Reynolds numbers are performed. Despite those localized differences mentioned above, the comparison between the critical flow points of the wake region presents a good harmony that can be seen between the two results.

3.2. Comparisons of wake flow structures and force coefficients

It can be seen from Table 4. that set the ground from a stationary wall to a translational moving boundary causes a slight drop in C_D . A similar result can be seen in references [9,27]. On the other hand, the just inclusion of the wheels and wheelhouses (SW+SG setup) results in a significant drag increment which is around 27.32% higher than the SG model. Contrary to the wheelless Ahmed body, the inclusion of moving ground causes a slight C_D increment of 0.41% for Ahmed body on wheels. This unexpected result will be explained when interpreting qualitative data later. Moreover, the addition of rotational speed to the wheel boundaries, namely MW+MG configuration, reduces C_D , yet the reduction is minor and approximately 1.29% compared with the SW+MG setup. The cause of the drag reduction is explained by the Coanda effect of rotating wheels as stated in [28].

As for C_L , the inclusion of moving ground results in reductions in C_L for both wheeled and wheelless configurations (by 34.8 and 37.7 counts, respectively). This can be explained by the increased venture effect of more induced airflow underbody. The inclusion of rotating wheels reduces C_L further by 54.5 counts compared with the SW+MG setup. This can be explained by the Coanda effect from the reference [28], too. Nevertheless, just the addition of wheels and wheel arches (SW+SG) results in C_L rise by 188.5 counts compared with SG setup even though wheels and ground are not moving.

Figure 7 presents the surface pressure contours at the front and rear parts of the body. The first salient difference between stationary and moving grounded setups can be seen at the rear end part. MG and SW+MG have lower surface pressure compared with the SG and SW+SG models, respectively. The lower pressure on the rear surface is in contrast with the drag reduction effect of moving ground boundary which has been mentioned previously, however, that result can be attributed to lower surface pressure in the front of the body of MG and SW+MG setups. However, all wheeled setups have remarkably higher surface pressure at the rear end, and this is not consistent with the higher C_D results of these setups compared with SG and MG setups. However, additional high-pressure zones caused by wheels and wheel housings that are in contact with the ground must create such a drag rise that is higher than the drag reduction effect of pressure recovery at the back of the body

surface. Nevertheless, no significant difference is observed between SW+MG and MW+MG setups neither in the front nor at the rear part.

In Figure 8, pressure coefficients (C_p) at the symmetry line of body surface ($z=0$) are represented for wheelless (SG and MG) and wheeled (SW+SG, SW+MG, and MW+MG) setups. Dashed and solid lines show the bottom and top surfaces of the bodies, respectively. For the wheelless configurations, no apparent difference can be seen except for bottom surfaces. The bottom surface of the MG has slightly lower C_p throughout the underbody, and this explains why the MG setup has lower C_L than the SG setup. When wheels and wheel housings are added to the body the main difference appears bottom surfaces of bodies specifically near the frontal surface and front wheels. A dramatic C_p rise occurs around this region which results in positive lift coefficients for all wheeled models. When comparisons are made among wheeled models, there is no major difference at the top surface of models while some differences stand out at bottom surfaces. In the front part of the bottom surface, the SW+SG model has higher surface pressure than other wheeled models. However, near the back SW+SG and SW+MG has similar trends whereas the MW+MG setup has lower pressure coefficients around there. This is one of the main differences that rotating wheels cause to C_L reduction in the body.

The turbulent kinetic energy (TKE) in the symmetry plane ($z=0$) is shown in Figure 9. Higher TKE is an indicator of higher energy dissipation which means greater energy loss due to drag. The difference between the contours of SG and MG setups is almost negligible except that MG has a slightly lower TKE at the lower part of the wake (red zone). Moving ground results in more airflow underbody and thus this airflow enables more energy which causes dissipation reduction. Considering MG and SW+SG setups, the TKE difference is more noticeable in almost the whole region of the wake than the difference between SG and MG. The presence of wheelhouses and wheels increases TKE values in the lower and upper regions of the wake for wheeled setups. The dissipation is significantly higher, and these results are consistent with the C_D values of the setups. Yet again the addition of moving ground to the wheeled model results in dissipation recovery at the lower wake and there is no significant difference between SW+SG and SW+MG models except that region. However, the difference between SW+MG and MW+MG could not be seen, so it can be said that the rotational speeds of wheels do not affect dissipation at the wake too much. Exceptionally, there are some minor rises in TKE values around the middle - near and upper regions for MW+MG setup compared with other wheeled setups, and this is contradictory to the slight C_D drop of this body. This can be interpreted as the wake and back part of the body is not responsible for relevant C_D change and there should be another reason for the drag decrement.

Locations of X_1 , X_2 , X_3 , X_4 , X_5 , and X_6 are illustrated in Figure 10 and given in Table 5 while normalized velocity (U/U_∞) contours of the cross-sectional planes of X_1 , X_2 , X_3 , X_4 , X_5 , and X_6 are shown in Figure 11. It can be said from the X_1 planes that moving ground is effective in increasing velocity around the underbody and sidewalls closer to the underbody for both wheelless and wheeled setups and this is the indication of more induced airflow. Nevertheless, there is no drastic difference in X_2 , X_3 , X_4 , X_5 , and X_6 sections of SG and MG configurations. For the wheeled models, some negligible velocity drops are observed with the inclusion of moving ground for the wheeled model. Regarding wheeled setups, velocity drops are remarkable around the wheels and the possible reason for the main drag difference between wheeled and wheelless models can be seen X_1 and X_2 sections of Figure 12. The velocity decrements can be seen even at the far wake (X_6) for wheeled setups. On the other hand, there is no apparent difference between SW+MG and MW+MG models. The most significant difference between these models is observed on the X_1 , X_2 , and X_3 planes. The streamwise velocity of the MW+MG setup specifically close to the wheels is slightly higher than SW+MG. This is possibly the cause of the relevant drag reduction effect of the rotational speed of wheels. It can be said that velocity decrement is considerable between the wheeled and wheelless models as can be seen from Figure 12. However, inclusions of rotational speed and moving ground to the numerical setups have negligible effects on the contours, respectively.

In Figure 13, normalized velocity (U/U_∞) contours at horizontal sections are presented and locations of Y_1 , Y_2 , and Y_3 sections can be seen from Figure 11 and Table 5. It can be said that there is no significant difference for all setups at the top plane (Y_1) whereas the differences become more apparent at lower sections. For wheelless models, the effects of the moving ground can only be seen at the lowest section (Y_3) and MG has a slightly narrower low-velocity zone than the SG setup. Just the addition of wheels and wheelhouses to the Ahmed body significantly widens the lower velocity region around the vehicle and wake. This change is more obvious for the Y_3 section. On the other hand, the addition of the moving ground to the wheeled model decreases velocity around the front wheel and the wake at Y_1 and Y_2 planes. These drops are possible reasons for the drag rise effect of moving ground for the wheeled model. Moreover, the addition of rotational speed of the wheels recovers these drops to some extent and this explains why wheel rotation reduces drag. The vortex-induced by wheels (as also reported by [10] and especially rear wheels) transmit some energy to the wake and a velocity recovery yields there.

In Figure 13, iso-surfaces of Q criterion for numerical setups of SG, MG, SW+SG, SW+MG, and MW+MG are illustrated. Q criterion is a vortex identification parameter used in fluid dynamics identified by Equation (1) [29].

$$Q = \frac{1}{2} (\|\Omega\|^2 - \|S\|^2) \quad (1)$$

where S is the rate of strain and Ω is the vorticity tensor. The iso-surfaces are created for $Q=4 \times 10^4 \text{ s}^{-2}$ in this study. This figure shows that the main difference between wheelless models is the MG setup has stronger vortical pairs at the side-lower part of the body and SG has some small vortex structures at the ground. On the other hand, the inclusion of wheels and wheelhouses to the Ahmed body strengthens vortices around the underbody and lower-side parts of the body significantly. Especially, large vortex structures can be seen around the front wheels. It can be said that moving ground and rotating wheels change the vortex formation of the wheeled Ahmed body slightly. The most apparent differences are that moving ground

extends vortices in the flow direction and reduces vortex intensity around the front wheels whereas rotating wheels increase the turbulence level of the flow and reduce side vortices. However, these differences are so minor that it cannot be said that there is a dramatic difference between wheeled setups.

4. CONCLUDING REMARKS

This study assesses the influence of the addition of moving ground, rotating wheels, and wheelhouses to an Ahmed body numerical simulation. Simulations have been conducted with the Ahmed body at a 35° slant angle with a k- ω SST turbulence model. For comparisons, C_D , C_L and the structure of wake regions were analyzed. According to the numerical investigation of this study following conclusions can be drawn for this slant angle:

- The inclusion of moving ground has little effect on the force coefficients and wake structure at 35° slant angle.
- The addition of rotating wheels and wheelhouses beside the moving ground has a minor effect on drag and flow pattern downstream of the Ahmed body with 35° slanted rear end.
- Wheels and wheelhouses create vortices and decrease velocity at the rear part of the Ahmed body and have some minor positive effects on the aerodynamic performance of the Ahmed body with 35°.
- Existence of wheels and wheelhouses causes significant lift increment whereas the inclusion of moving and rotating boundaries reduces lift force.
- The inclusion of rotational speed to the wheeled Ahmed body model has a comparably lower effect on the drag coefficient. Hence, the stationary wheel and ground setup can be preferred for experimental studies which do not have rotating wheel and moving ground mechanism facilities.
- In the future work, more realistic generic models can be used such as DrivAer and AeroSUV. Also, different behavior of the passive control elements on the wheeled and wheelless model can be investigated deeply.

Declarations

No conflict of interest was declared by the authors.

Acknowledgments

The authors wish to express thanks to the Department of Energy Systems Engineering of Osmaniye Korkut Ata University for the possibility to support their CFD Software and many thanks go to the software provider ANSYS Fluent™.

References

1. Katz, J., *AUTOMOTIVE AERODYNAMICS*, John Wiley & Sons, Ltd. (2016).
2. Wang, Y., Wu, C., Tan, G., et al. "Reduction in the aerodynamic drag around a generic vehicle by using a non-smooth surface", *Proc. Inst. Mech. Eng. Part D J. Automob. Eng.*, **231**(1), pp. 130–144 (2017).
3. Morel, T., "Effect of Base Slant on the Flow Pattern and Drag of Three-Dimensional Bodies With Blunt Ends.", *Aerodyn. Drag Mech. Bluff Bodies Road Veh. Springer, Boston, MA*, pp. 191–226 (1978).
4. Ahmed, S. R., Ramm, G., and Faltin, G., "Some salient features of the time-averaged ground vehicle wake", *SAE Tech. Pap.* (1984).
5. Dobrev, I. and Massouh, F., "Investigation of relationship between drag and lift coefficients for a generic car model", *BULTRANS-2014*, pp. 171–174 (2014).
6. Sumida, M. and Hayakawa, K., "Aerodynamic forces acting on Ahmed-type vehicles under fluctuating headwind conditions", *J. Appl. Fluid Mech.*, **12**(5), pp. 1563–1574 (2019).
7. Meile, W., Brenn, G., Reppenhagen, A., et al. "Experiments and numerical simulations on the aerodynamics of the ahmed body", *CFD Lett.*, **3**(1), pp. 32–38 (2011).
8. Bayraktar, I., Landman, D., and Baysal, O., *Experimental and Computational Investigation of Ahmed Body for Ground Vehicle Aerodynamics* (2001).
9. Strachan, R. K., Knowles, K., and Lawson, N. J., "The vortex structure behind an Ahmed reference model in the presence of a moving ground plane", *Exp. Fluids*, **42**(5), pp. 659–669 (2007).
10. Gulyás, A., Bodor, Á., Regert, T., et al. "PIV measurement of the flow past a generic car body with wheels at LES applicable Reynolds number", *Int. J. Heat Fluid Flow*, **43**, pp. 220–232 (2013).
11. Huminic, A. and Huminic, G., "Aerodynamic study of a generic car model with wheels and underbody diffuser", *Int. J. Automot. Technol.*, **18**(3), pp. 397–404 (2017).
12. Wang, S., Avadiar, T., Thompson, M. C., et al. "Effect of moving ground on the aerodynamics of a generic automotive model: The DrivAer-Estate", *J. Wind Eng. Ind. Aerodyn.*, **195**, p. 104000 (2019).
13. Krajnović, S. and Davidson, L., "Influence of floor motions in wind tunnels on the aerodynamics of road vehicles", *J. Wind Eng. Ind. Aerodyn.*, **93**(9), pp. 677–696 (2005).
14. Krajnovic, S., Sarmast, S., and Basara, B., "Numerical investigation of the flow around a simplified wheel in a wheelhouse", *J. Fluids Eng. Trans. ASME*, **133**(11) (2011).
15. Zhou, H., Qin, R., Wang, G., et al. "Comparative analysis of the aerodynamic behavior on Ahmed body mounted with different wheel configurations", *Proc. Inst. Mech. Eng. Part D J. Automob. Eng.* (2022).
16. Aljure, D., Lehmkuhl, O., Favre, F., et al. "On the IBM Approximation for the Wheel Aerodynamic Simulation" In *Proceedings of the First International Conference in Numerical and Experimental Aerodynamics of Road Vehicles and Trains (Aerovehicles 1)*, Bordeaux, France, pp. 23–25(2014).
17. Regert, T. and Lajos, T., "Description of flow field in the wheelhouses of cars", *Int. J. Heat Fluid Flow*, **28**(4), pp. 616–629 (2007).

18. Menter, F., “Improved two-equation k-omega turbulence models for aerodynamic flows”, *NASA Tech. Memo.*, (103978), pp. 1–31 (1992).
19. Siddiqui, N. A. and Chaab, M. A., “A Simple Passive Device for the Drag Reduction of an Ahmed Body”, *J. Appl. Fluid Mech.*, **14**(1), pp. 147–164 (2020).
20. Guilmineau, E., Deng, G. B., Leroyer, A., et al. “Assessment of hybrid RANS-LES formulations for flow simulation around the Ahmed body”, *Comput. Fluids*, **176**, pp. 302–319 (2018).
21. Zhang, C., Bounds, C. P., Foster, L., et al. “Turbulence modeling effects on the CFD predictions of flow over a detailed full-scale sedan vehicle”, *Fluids*, **4**(3) (2019).
22. Mohammadikalakoo, B., Schito, P., and Mani, M., “Passive flow control on Ahmed body by rear linking tunnels”, *J. Wind Eng. Ind. Aerodyn.*, **205** (2020).
23. Davidson, L., “Assessment of Turbulence Models for Flow Simulation Around the Ahmed Body”, *Annu. Rev. Fluid Mech.*, **32**(1), pp. 1–32 (2016).
24. Lienhart, H. and Becker, S., *Flow and Turbulence Structure in the Wake of a Simplified Car Model* (2003).
25. Avadiar, T., Thompson, M. C., Sheridan, J., et al. “Characterisation of the wake of the DrivAer estate vehicle”, *J. Wind Eng. Ind. Aerodyn.*, **177**, pp. 242–259 (2018).
26. Tunay, T., Firat, E., and Sahin, B., “Experimental investigation of the flow around a simplified ground vehicle under effects of the steady crosswind”, *Int. J. Heat Fluid Flow*, **71**, pp. 137–152 (2018).
27. Krajnović, S. and Davidson, L., “Flow around a simplified car, part 2: Understanding the flow”, *J. Fluids Eng. Trans. ASME*, pp. 919–928 (2005).
28. Kang, S.-O., Jun, S.-O., Park, H. H.-I., et al. “Influence of Rotating Wheel and Moving Ground Condition to Aerodynamic Performance of 3-Dimensional Automobile Configuration”, *Trans. Korean Soc. Automot. Eng.*, **18**(5), pp. 100–107 (2010).
29. Jeong, J. and Hussain, F., “On the identification of vortex”, *J. Fluid Mech.*, **285**, pp. 69–94 (1995).

Figure 1. Ahmed body on wheels, dimensions in mm

Figure 2. The view of mesh elements

Table 1. Meshing strategy of this numerical study

Figure 3. Mesh independence study

Figure 4. Dimensions and boundary conditions of the computational domain

Table 2 Boundary conditions setups for numerical configurations of this study

Table 3 Computational domain properties

Table 4. Comparison of force coefficients of CFD setups with the experimental data

Figure 5. Comparison of dimensionless x-directional velocities at the line of $y/H=1.065$ ($z=0$)

Figure 6 Velocity streamlines at the symmetry plane and the location plot of critical points

Figure 7. Surface pressure contours in the front (left) and at the rear (right) part of the body

Figure 8. Pressure coefficients at symmetry ($z=0$)

Figure 9. TKE contours in the wake region

Figure 10. Cross-sectional planes that are used investigate the flow field

Table 5 Locations of the planes

Figure 11. Normalized velocity (U/U_∞) contours at cross-sections of the domain (from top to bottom: X_1 , X_2 , X_3 , X_4 , X_5 , and X_6)

Figure 12. Normalized velocity (U/U_∞) contours at horizontal sections of the domain (from top to bottom: Y_1 , Y_2 , and Y_3)

Figure 13 Iso-surfaces of $Q=4 \times 10^4 \text{ s}^{-2}$ for the numerical setups

Abbreviations

A	The frontal area of the body (m ²)	Re	Reynolds Number
C _D	Drag coefficient	TKE	Turbulent kinetic energy (m ² /s ²)
C _f	Drag coefficient caused by friction drag	U	Local flow velocity (m/s)
C _L	Lift coefficient	U _∞	Free stream velocity (m/s)
C _p	Drag coefficient caused by pressure drag	y+	Dimensionless wall coordinate
k	Turbulence kinetic energy per unit mass (m ² /s ²)	ΔC_D	Deviation of drag coefficient result from the SG setup (%)
L	Body length (mm)	ρ	Density (kg/m ³)
RANS	Reynolds-Averaged Navier-Stokes	ω	Turbulence eddy frequency (s ⁻¹)

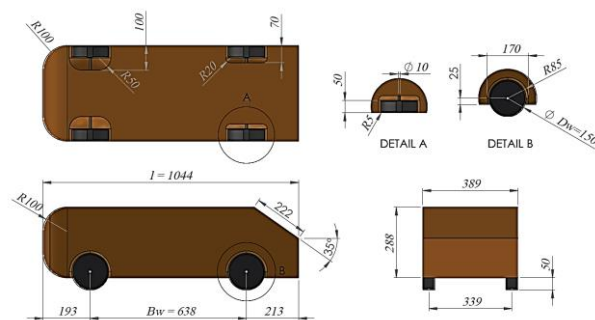


Figure 14. Ahmed body on wheels, dimensions in mm

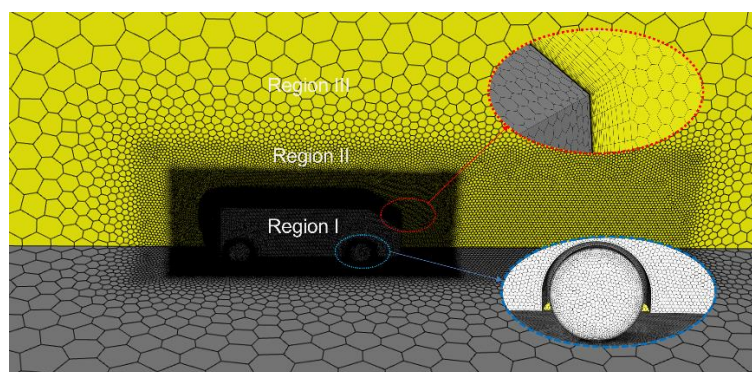


Figure 15. The view of mesh elements

Table 6. Meshing strategy of this numerical study

	Mesh 1	Mesh 2	Mesh 3	Mesh 4
Element size of the region I (mm)	20	7.5	6.25	5
Element size of region II (mm)	40	17.5	17.5	15
Global element size (region III) (mm)	250	175	150	150
First prism layer height (mm)	0.05	0.05	0.05	0.05
Number of prism layer	25	25	25	25
Growth rate	1.2	1.2	1.2	1.2
Volume mesh type	Poly-hexcore	Poly-hexcore	Poly-hexcore	Poly-hexcore
Total mesh count (x10 ⁶)	1.2	1.98	3.08	3.96

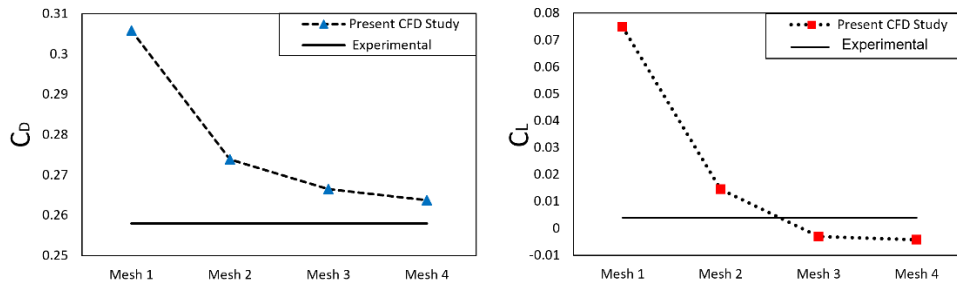


Figure 3. Mesh independence study

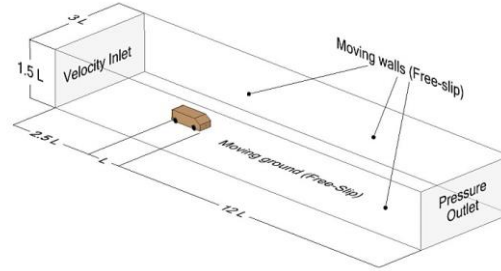


Figure 4. Dimensions and boundary conditions of the computational domain

Table 7. Boundary conditions setups for numerical configurations of this study

Boundary Conditions					
	SG	MG	SW+SG	SW+MG	MW+MG
Inlet	Velocity Inlet (40 m/s)	Velocity Inlet (40 m/s)	Velocity Inlet (40 m/s)	Velocity Inlet (40 m/s)	Velocity Inlet (40 m/s)
Outlet	Pressure outlet (0 Pa)	Pressure outlet (0 Pa)	Pressure outlet (0 Pa)	Pressure outlet (0 Pa)	Pressure outlet (0 Pa)
Vehicle surface	No-slip	No-slip	No-slip	No-slip	No-slip
Wheels	No-wheels included	No-wheels included	No-slip	No-slip	Moving wall - Rotational (533.3 rad/s)
Top and sidewalls	Free-slip	Free-slip	Free-slip	Free-slip	Free-slip
Floor	No-slip	Moving wall-Sliding (40 m/s)	Stationary wall (No-slip)	Moving wall-Sliding (40 m/s)	Moving wall - Sliding (40 m/s)

Table 8. Computational domain properties

Computational Domain	
Flow Field	quasi-3D, steady, turbulent, and incompressible flow
Length X width X height	15.5L X 3L X 1.5L (16182 mm X 3102 mm X 1566 mm)
Vehicle cross-sectional area	112032 mm ² (SG and MG) 117022.365 mm ² (SW+SG, SW+MG and MW+MG)
Blockage ratio	2.386%

Table 9. Comparison of force coefficients of CFD setups with the experimental data

	Experimental SG [4]	Experimental SG [7]	Experimental MG [9]	Numerical MW+MG [11]	SG	MG	SW+SG	SW+MG	MW+MG
C_D	0.2580	0.2790	0.2700	0.3420	0.2664	0.257	0.3392	0.3406	0.3362
C_L	n.a.	0.0040	-0.05	0.1470	0.0053	-0.0295	0.1938	0.1561	0.1016

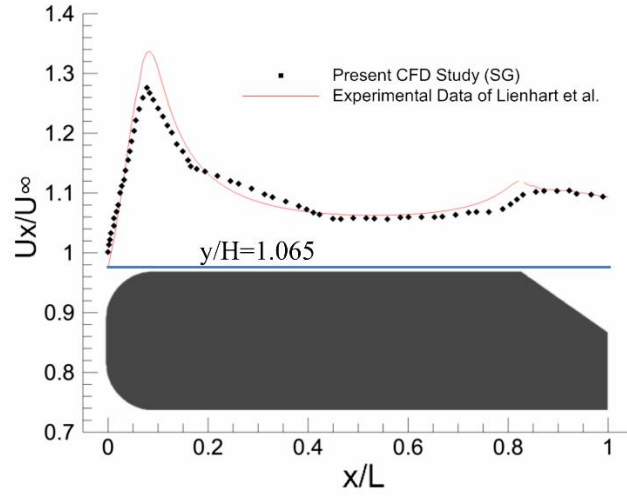


Figure 5. Comparison of dimensionless x-directional velocities at the line of $y/H=1.065$ ($z=0$)

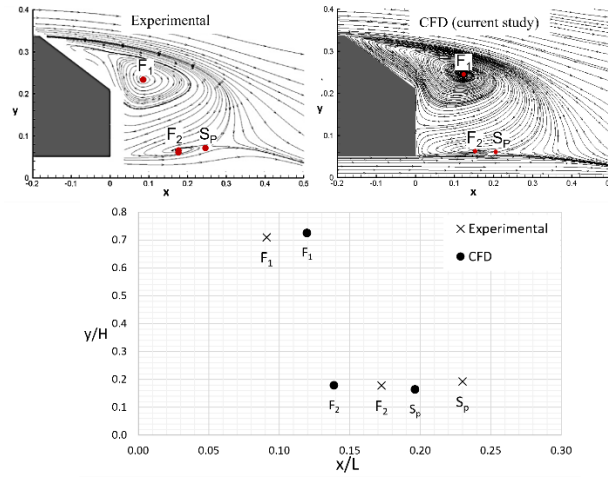


Figure 6. Velocity streamlines at the symmetry plane and the location plot of critical points

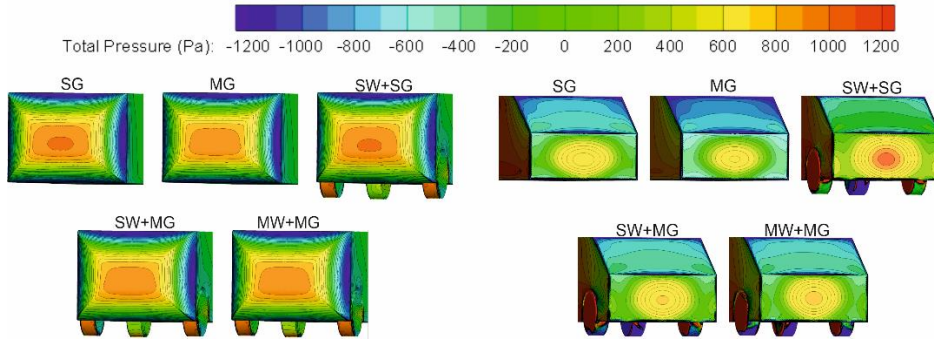


Figure 7. Surface pressure contours in the front (left) and at the rear (right) part of the body

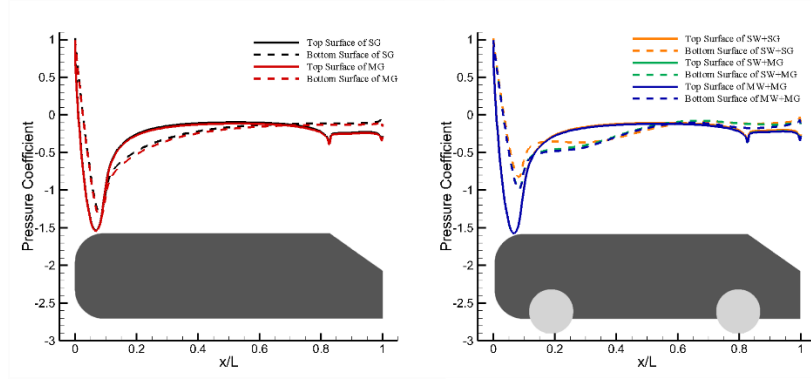


Figure 8. Pressure coefficients at symmetry ($z=0$)

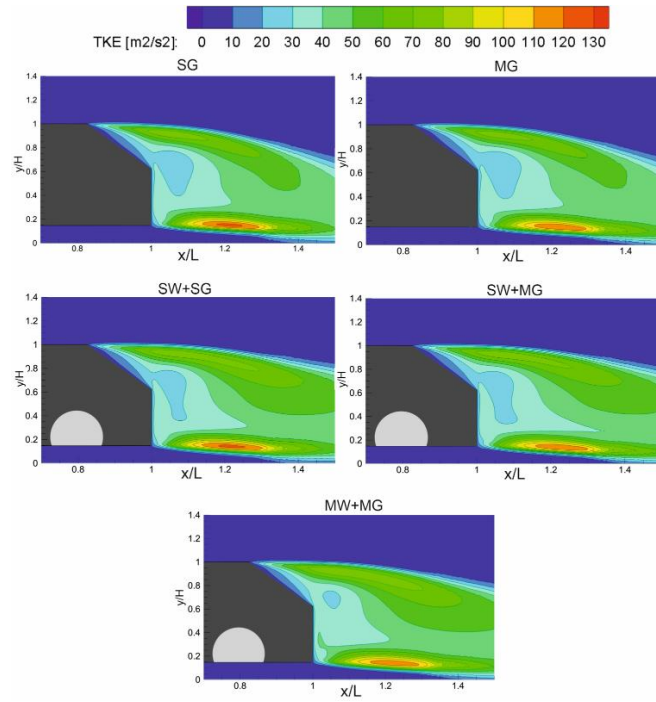


Figure 9. TKE contours in the wake region

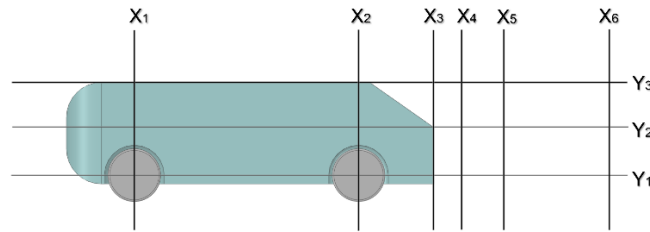


Figure 16. Cross-sectional planes that are used to investigate the flow field

Table 10. Locations of the planes

Location		Location		Location	
X ₁	x/L=0.18	X ₄	x/L=1.08	Y ₁	y/H=1
X ₂	x/L=0.80	X ₅	x/L=1.19	Y ₂	y/H=0.62
X ₃	x/L=1	X ₆	x/L=1.48	Y ₃	y/H=0.22

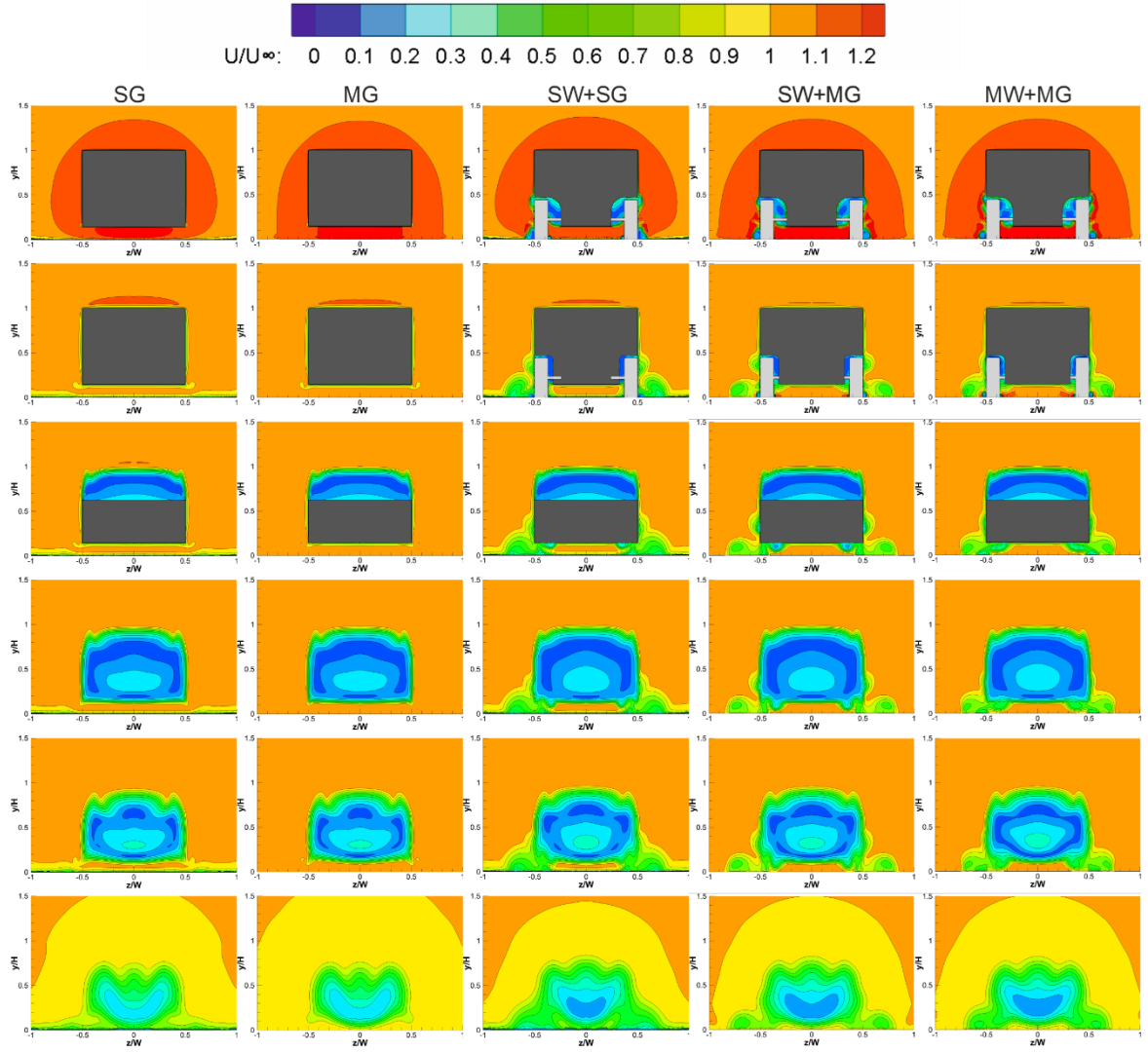


Figure 11. Normalized velocity (U/U_∞) contours at cross-sections of the domain (from top to bottom: X_1, X_2, X_3, X_4, X_5 , and X_6)

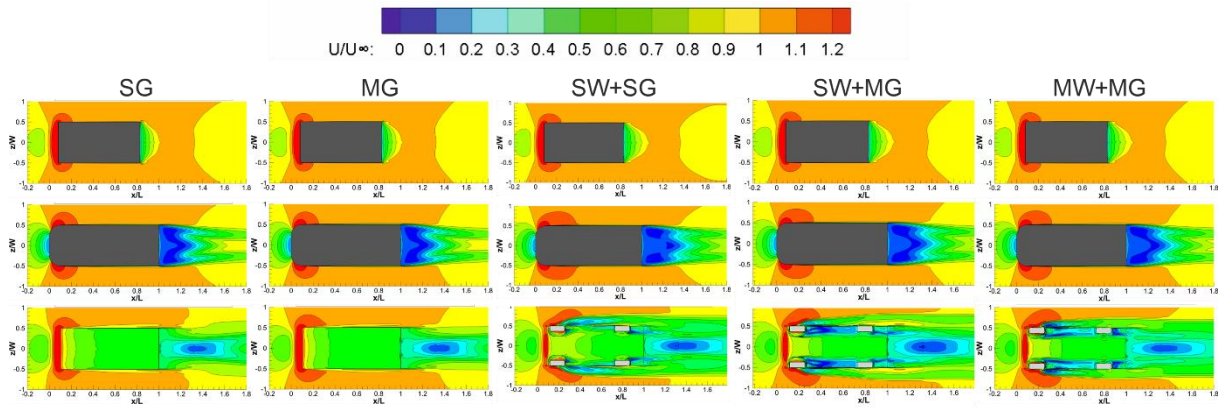


Figure 17. Normalized velocity (U/U_∞) contours at horizontal sections of the domain (from top to bottom: Y_1, Y_2 , and Y_3)

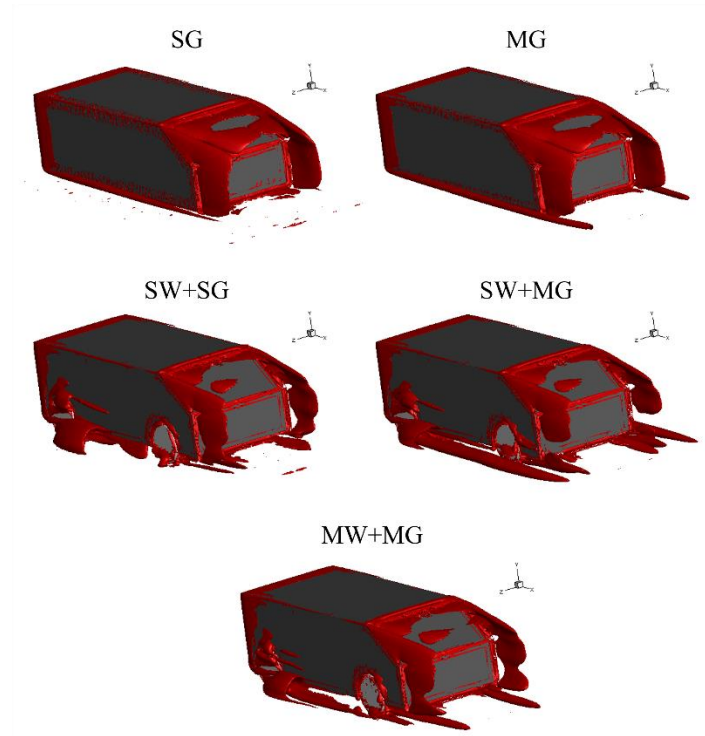


Figure 18. Iso-surfaces of $Q=4 \times 10^4 \text{ s}^{-2}$ for the numerical setups

Biographies

Sinan Keiyinci is a Research Assistant at the Department of Automotive Engineering, Çukurova University. He has non-academic experience in Turkish Airlines as Business Establishment Private between 2011-2022. He completed his BSc and MSc degrees in the Civil Aviation Department of Erciyes University, Kayseri and his PhD in 2021 at the University of Çukurova, Automotive Engineering Department. He is interested in alternative energy systems, aerodynamics and EV batteries.

Oğuz Baş is a research assistant at Thermodynamic Department of Mechanical Engineering of Amasya University. He worked in SANKO Construction Machinery Factory as a R&D engineer in 2015. He received MSc in 2018 and PhD in 2023 from Automotive Engineering Department of Çukurova University. He has papers in alternative fuel usage in ICE such as biodiesel, alcohols as well as computational and experimental vehicle aerodynamics. He is currently studying computational and experimental automotive aerodynamics.

Mustafa Atakan Akar is a faculty member at the Department of Mechanical Engineering, Çukurova University, Turkey. In 1999, he received a BSc degree at the Mechanical Engineering Department, from Çukurova University. He received MSc (2003) and PhD (2008) degrees at the Mechanical Engineering Department from Çukurova University. He has been working as an Associated Professor at Çukurova University since 2018. He has many scientific studies on experimental fluid dynamics in water channel, internal combustion engines, alternative fuels, and automotive aerodynamics.